

# Computation of electron diffraction patterns in Lorentz electron microscopy of thin magnetic films

Cite as: Journal of Applied Physics **69**, 2455 (1991); <https://doi.org/10.1063/1.348682>

Submitted: 14 June 1990 . Accepted: 20 November 1990 . Published Online: 17 August 1998

M. Mansuripur



View Online



Export Citation

## ARTICLES YOU MAY BE INTERESTED IN

### The design and verification of MuMax3

AIP Advances **4**, 107133 (2014); <https://doi.org/10.1063/1.4899186>

### Mapping the magnetization fine structure of a lattice of Bloch-type skyrmions in an FeGe thin film

Applied Physics Letters **111**, 192410 (2017); <https://doi.org/10.1063/1.5004394>

### Determination of domain wall chirality using in situ Lorentz transmission electron microscopy

AIP Advances **7**, 056807 (2017); <https://doi.org/10.1063/1.4977500>

## Ultra High Performance SDD Detectors



See all our XRF Solutions

# Computation of electron diffraction patterns in Lorentz electron microscopy of thin magnetic films

M. Mansuripur

*Optical Sciences Center, University of Arizona, Tucson, Arizona 85721*

(Received 14 June 1990; accepted for publication 20 November 1990)

The vector potential field for a thin magnetic film with arbitrary pattern of magnetization is calculated using fast Fourier transforms. The vector potential is used to compute the phase modulation imparted to the electron beam in Lorentz electron microscopy. Calculated phase patterns and the corresponding intensity distributions for several magnetic configurations of practical interest are described.

## I. INTRODUCTION

Lorentz electron microscopy is a powerful tool for high-resolution studies of magnetic structure in thin films.<sup>1-6</sup> The physical mechanism that underlies all known modes of Lorentz microscopy is the interaction between the propagating electron wave and the magnetic vector potential field. For a given electron trajectory, the interaction, commonly known as the Aharonov-Bohm effect, results in a phase delay directly proportional to the path integral of the vector potential.<sup>7</sup> Lorentz microscopy is therefore a branch of phase-contrast microscopy whose various modes (e.g., Fresnel, Foucault, Differential Phase Contrast, Small Angle Diffraction, Electron Interference, and Holography) simply represent different designs for capturing the information contained in the phase of the beam after passage through a magnetic specimen. The purpose of the present paper is to introduce a general technique for computing the phase imparted to the electron beam by an arbitrary two-dimensional pattern of magnetization. In Sec. II we establish the mathematical relation between the magnetization distribution and the vector potential field. Numerical results obtained with the proposed scheme are then presented in Sec. III.

## II. MATHEMATICAL ANALYSIS

In a previous paper<sup>8</sup> we showed that the magnetic field distribution  $H(x,y,z)$  of a thin magnetic film can be accurately and efficiently computed with the aid of fast Fourier transforms. That work is now extended to the computation of the vector potential field  $A(x,y,z)$ . Consider a magnetic film parallel to the  $xy$  plane of a Cartesian coordinate system, as shown in Fig. 1, and denote its magnetization distribution by  $\mathbf{m}(x,y)$ . Assume that the film has thickness  $\tau$  and that its surfaces are at  $z = \pm\tau/2$ . Also assume that  $\mathbf{m}(x,y)$  is periodic along both  $x$  and  $y$ , with periods being  $L_x$  and  $L_y$ , respectively. Thus the Fourier series representation of the film's magnetization will be

$$\mathbf{m}(x,y) = \sum_{m=-\infty}^{\infty} \sum_{n=-\infty}^{\infty} \mathbf{M}_{mn} \exp \left[ i2\pi \left( \frac{mx}{L_x} + \frac{ny}{L_y} \right) \right], \quad (1a)$$

where

$$\mathbf{M}_{mn} = \frac{1}{L_x L_y} \int_0^{L_x} \int_0^{L_y} \mathbf{m}(x,y) \exp \left[ -i2\pi \left( \frac{mx}{L_x} + \frac{ny}{L_y} \right) \right] dx dy. \quad (1b)$$

In general, an arbitrary magnetization distribution  $\mathbf{m}(\mathbf{r})$  gives rise to the vector potential field  $\mathbf{A}(\mathbf{r})$  described by the convolution integral

$$\mathbf{A}(\mathbf{r}) = \int \int \int_{-\infty}^{\infty} \mathbf{m}(\mathbf{r}') \times \frac{\mathbf{r} - \mathbf{r}'}{|\mathbf{r} - \mathbf{r}'|^3} d^3r'. \quad (2)$$

In the case of a thin film whose magnetization could be assumed uniform through the thickness,  $\mathbf{m}(\mathbf{r})$  may be written as  $\mathbf{m}(x,y)u(z)$ , where

$$u(z) = \begin{cases} 1; & |z| < \frac{\tau}{2} \\ 0; & \text{Otherwise.} \end{cases} \quad (3)$$

Now, the Fourier transform operators in 2 and 3 dimensions are

$$\begin{aligned} \mathcal{F}_2\{\mathbf{g}(x,y)\} &= \mathbf{G}(s_x, s_y) \\ &= \int \int_{-\infty}^{\infty} \mathbf{g}(x,y) \\ &\quad \times \exp[-i2\pi(xs_x + ys_y)] dx dy \end{aligned} \quad (4a)$$

and

$$\begin{aligned} \mathcal{F}_3\{\mathbf{g}(x,y,z)\} &= \mathbf{G}(s_x, s_y, s_z) \\ &= \int \int \int_{-\infty}^{\infty} \mathbf{g}(x,y,z) \times \exp \\ &\quad [ -i2\pi(xs_x + ys_y \\ &\quad + zs_z) ] dx dy dz. \end{aligned} \quad (4b)$$

Accordingly, one may write the Fourier transform of Eq. (2) as follows:

$$\mathcal{F}_3\{\mathbf{A}(\mathbf{r})\} = \mathcal{F}_3\{\mathbf{m}(\mathbf{r})\} \times \mathcal{F}_3\left\{ \frac{\mathbf{r}}{|\mathbf{r}|^3} \right\}. \quad (5)$$

The Fourier transforms on the right side of Eq. (5) can be shown to be

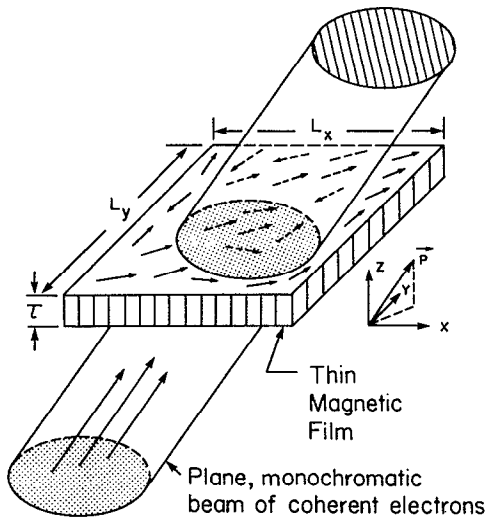


FIG. 1. Schematic drawing of the magnetic film and the electron beam in Lorentz electron microscopy.  $xy$  is the plane of the film and the unit vector  $\mathbf{p}$  is the propagation direction of the beam.

$$\mathcal{F}_3\{\mathbf{m}(\mathbf{r})\} = \frac{i}{2\pi s_z} [\exp(-i\pi\tau s_z) - \exp(i\pi\tau s_z)] \mathcal{F}_2\{\mathbf{m}(x,y)\}, \quad (6)$$

and

$$\mathcal{F}_3\left\{\frac{\mathbf{r}}{|\mathbf{r}|^3}\right\} = -\frac{2is}{|s|^2}. \quad (7)$$

Consequently,

$$\mathbf{A}(x,y,z) = \int \int_{-\infty}^{\infty} \mathcal{F}_2\{\mathbf{m}(x,y)\} \times \mathbf{Q}_z(s_x, s_y) \exp[i2\pi(x s_x + y s_y)] ds_x ds_y, \quad (8a)$$

where

$$\mathbf{Q}_z(s_x, s_y) = \int_{-\infty}^{\infty} \frac{\exp[i2\pi(z - \tau/2)s_z] - \exp[i2\pi(z + \tau/2)s_z]}{\pi s_z (s_x^2 + s_y^2 + s_z^2)} \mathbf{s} ds_z. \quad (8b)$$

The integrals in Eq. (8b) are readily evaluated using the identities

$$\int_{-\infty}^{\infty} \frac{\exp(i2\pi\xi s)}{\pi s (a^2 + s^2)} ds = \frac{i\xi}{a^2|\xi|} [1 - \exp(-2\pi a|\xi|)]; \quad a > 0, \quad (9)$$

and

$$\int_{-\infty}^{\infty} \frac{\exp(i2\pi\xi s)}{\pi (a^2 + s^2)} ds = \frac{1}{a} \exp(-2\pi a|\xi|); \quad a > 0. \quad (10)$$

Replacing for  $\mathbf{m}(x,y)$  in Eq. (8a) from Eq. (1) and carrying out the integrals, one obtains

$$\mathbf{A}(x,y,z) = \sum_{m=-\infty}^{\infty} \sum_{n=-\infty}^{\infty} \mathbf{A}_{mn}(z) \exp\left[i2\pi\left(\frac{mx}{L_x} + \frac{ny}{L_y}\right)\right], \quad (11a)$$

where

$$\mathbf{A}_{mn}(z) = \begin{cases} \frac{2i}{s} \exp(+2\pi s z) \sinh(\pi\tau s) \sigma_- \times \mathbf{M}_{mn} & z < -\frac{\tau}{2} \\ \frac{2i}{s} \left[ \sigma_- - \frac{1}{2} \exp[2\pi s(z - \tau/2)] \sigma_- - \frac{1}{2} \right. \\ \quad \left. \times \exp[-2\pi s(z + \tau/2)] \sigma_+ \right] \times \mathbf{M}_{mn} & |z| < \frac{\tau}{2} \\ \frac{2i}{s} \exp(-2\pi s z) \sinh(\pi\tau s) \sigma_+ \times \mathbf{M}_{mn} & z > +\frac{\tau}{2} \end{cases}$$

In the above equation  $s$  is the magnitude of the 2-dimensional frequency vector  $\mathbf{s}$ , defined as

$$\mathbf{s} = s_x \hat{x} + s_y \hat{y} = (m/L_x) \hat{x} + (n/L_y) \hat{y}, \quad (11c)$$

$\sigma$  is a unit vector along  $\mathbf{s}$ , namely,

$$\sigma = (s_x/s) \hat{x} + (s_y/s) \hat{y}, \quad (11d)$$

and  $\sigma_+$  and  $\sigma_-$  are complex vectors defined as:

$$\sigma_{\pm} = \sigma \pm i \hat{z}. \quad (11e)$$

The term corresponding to  $m = n = 0$  in Eq. (11b) is obtained by setting  $\sigma = 0$  and allowing  $s$  to approach zero. One finds

$$A_{00}(z) = \begin{cases} +2\pi\tau \hat{z} \times \mathbf{M}_{00} & z < -\tau/2 \\ -4\pi z \hat{z} \times \mathbf{M}_{00} & |z| < \tau/2 \\ -2\pi\tau \hat{z} \times \mathbf{M}_{00} & z > +\tau/2 \end{cases} \quad (11f)$$

Equation (11) is a general expression for the vector potential field of thin magnetic films, with the stipulation that the magnetization through the film thickness is uniform.

To find the phase modulation imparted to the electron beam after passage through the magnetic film, we must integrate  $\mathbf{A}(x,y,z)$  along the electron trajectories. As indicated in Fig. 1, the unit vector  $\mathbf{p}$  denotes the direction of propagation of the beam. The imparted phase function  $\Phi(x,y)$  is thus given by<sup>1</sup>

$$\Phi(\mathbf{r}) = \frac{e}{\hbar c} \int_{-\infty}^{\infty} \mathbf{p} \times \mathbf{A}(\mathbf{r} + \ell \mathbf{p}) d\ell. \quad (12)$$

In Eq. (12)  $\mathbf{r} = (x \hat{x} + y \hat{y})$  is the intersection of an arbitrary electron trajectory with the  $xy$  plane at  $z = 0$ ,  $e$  is the electronic charge,  $\hbar$  is Planck's constant, and  $c$  is the speed of light. Replacing for  $\mathbf{A}$  from Eq. (11) and evaluating the integral in Eq. (12) we obtain

$$\Phi(x,y) = \frac{2e}{\hbar c} \sum_{m=-\infty}^{\infty} \sum_{\substack{n=-\infty \\ mn \neq 00}}^{\infty} i \frac{\tau}{s} G_p(\tau s) (\sigma \times \hat{z}) \cdot [\mathbf{p} \times (\mathbf{p} \times \mathbf{M}_{mn})] \exp \left[ i 2\pi \left( \frac{mx}{L_x} + \frac{ny}{L_y} \right) \right], \quad (13a)$$

where

$$G_p(\tau s) = \frac{1}{(\mathbf{p} \cdot \sigma)^2 + (\mathbf{p} \cdot \hat{z})^2} \frac{\sin(\pi \tau s \mathbf{p} \cdot \sigma / \mathbf{p} \cdot \hat{z})}{\pi \tau s \mathbf{p} \cdot \sigma / \mathbf{p} \cdot \hat{z}}. \quad (13b)$$

Some of the more interesting features of this phase function will now be described.

(i) The factor  $1/s$  in Eq. (13a) appears to discriminate against high spatial frequencies. This appearance however is deceiving. The local deflection of the electron beam is proportional to the gradient of the phase function. Since for a sinusoidal function the gradient is proportional to the frequency, the  $1/s$  factor maintains the balance amongst the various Fourier components in their contributions to the deflection of the electrons.

(ii) In the expression for  $\Phi(x,y)$  all Fourier components  $\mathbf{M}_{mn}$  of the magnetization distribution appear as  $\mathbf{p} \times (\mathbf{p} \times \mathbf{M}_{mn})$ . Since  $\mathbf{p}$  is a constant unit vector, one might as well begin the analysis by Fourier transforming  $\mathbf{p} \times [\mathbf{p} \times \mathbf{m}(x,y)]$  instead of  $\mathbf{m}(x,y)$ . In this way it immediately becomes clear that the projection of  $\mathbf{m}(x,y)$  along the propagation direction  $\mathbf{p}$  makes no contribution to  $\Phi(x,y)$ . What is more, since in Eq. (13a) the vector  $\sigma \times \hat{z}$  is dot multiplied by the Fourier coefficients of  $\mathbf{p} \times [\mathbf{p} \times \mathbf{m}(x,y)]$ , the latter vector's component along the  $z$  axis plays no role in the outcome and may also be discarded. One thus retains only the components of  $\mathbf{p} \times [\mathbf{p} \times \mathbf{m}(x,y)]$  along the  $x$  and  $y$  axes for further processing.

(iii) The part of the magnetization distribution  $\mathbf{m}(x,y)$  which survives the initial processing steps described above, may still fail to contribute to  $\Phi(x,y)$ . For instance, if  $\mathbf{p} \times (\mathbf{p} \times \mathbf{M}_{mn})$  happens to be parallel to its corresponding frequency vector  $\sigma$ , the dot product in Eq. (13a) vanishes. Thus the various spatial frequencies contained in the magnetization pattern receive unequal representation in the phase function.

(iv) When the electron beam is normally incident on the sample (i.e., when  $\mathbf{p} = \hat{z}$ ) the function  $G_p(\tau s)$  is equal to unity for all spatial frequencies  $s$ . At all other angles of incidence,  $G_p(\tau s)$  attenuates certain spatial frequencies relative to others. Notice that the film thickness  $\tau$  appears in  $G_p(\tau s)$  only as a scaling factor for  $s$ . Thus for a given magnetization distribution and a given (oblique) direction of incidence, thinner films convey the information content of the high-frequency terms better than thick films.

(v) The zero-frequency term  $\mathbf{M}_{00}$  does not appear in Eq. (13), indicating that a uniformly magnetized film will cause no deflection of the electron beam. This is contrary to our expectations based on the Lorentz law of force, which predicts a net deflection angle proportional to the in-plane component of magnetization. Inspection of the zero-frequency term  $\mathbf{A}_{00}$  in Eq. (11f), however, reveals

that this term is an odd function of  $z$ . Thus the part of the path within the region  $z < 0$  cancels the contribution to the phase made by the part that lies in  $z > 0$ . Of particular interest here is the case of normal incidence (i.e.,  $\mathbf{p} = \hat{z}$ ) where the zero-frequency vector potential everywhere in space is orthogonal to the path, making no contribution whatsoever to the phase function. The absence of the zero-frequency term from the phase function, however, has no practical significance, since in practice the sample dimensions are always finite and the zero-frequency term is inevitably replaced by low-frequency terms which continue to obey the Lorentz law of force.

### III. NUMERICAL RESULTS AND DISCUSSION

To gain a better understanding of the numbers involved in Lorentz microscopy, let us first consider the simple case of a magnetic film whose in-plane magnetization (oriented along  $y$ ) has the following distribution:

$$\mathbf{m}(x,y) = M_s \cos(2\pi x/L_x) \hat{y}. \quad (14a)$$

Provided that  $L_x$  is sufficiently large, this magnetization will appear uniform in the vicinity of the origin.  $\Phi(x,y)$  for the above distribution is readily computed from Eq. (13). Assuming that the electron beam is normally incident, one finds

$$\Phi(x,y) = - \frac{2e\tau M_s \sin(2\pi x/L_x)}{\hbar c} \frac{1}{L_x}. \quad (14b)$$

If the electron beam is confined to the neighborhood of the origin, one may replace the sine function in Eq. (14b) with its argument to obtain

$$\Phi(x,y) \approx - \frac{4\pi e\tau M_s}{\hbar c} x. \quad (14c)$$

In the Gaussian system of units  $e = 4.80325 \times 10^{-10}$  esu,  $c = 2.99793 \times 10^{10}$  cm/s, and  $\hbar = 1.05459 \times 10^{-27}$  erg sec. For a film of thickness  $\tau = 600 \text{ \AA}$  and saturation magnetization  $M_s = 1000 \text{ emu/cm}^3$  the phase of the electron beam upon transmission through the sample is therefore given by

$$\Phi(x,y) = - 1.146 \times 10^6 x, \quad (14d)$$

where the units are centimeter for  $x$  and radian for  $\Phi$ .

Let the kinetic energy of the electron beam be  $E_k = 100 \text{ keV}$ . Then the electron wavelength  $\lambda$  is computed from the formula

$$\lambda = h / \sqrt{2mE_k + (E_k/c)^2}. \quad (15)$$

to be  $0.037 \text{ \AA}$ . [In Eq. (15)  $h$  is Planck's constant and  $m$  is the electron mass. The expression in the denominator gives the momentum of the electron, including the relativistic correction to the classical momentum-energy relation.] The phase function in Eq. (14d) may now be written as follows:

$$\Phi(x,y) = \frac{2\pi}{\lambda} (67.5 \times 10^{-6}) x. \quad (16)$$

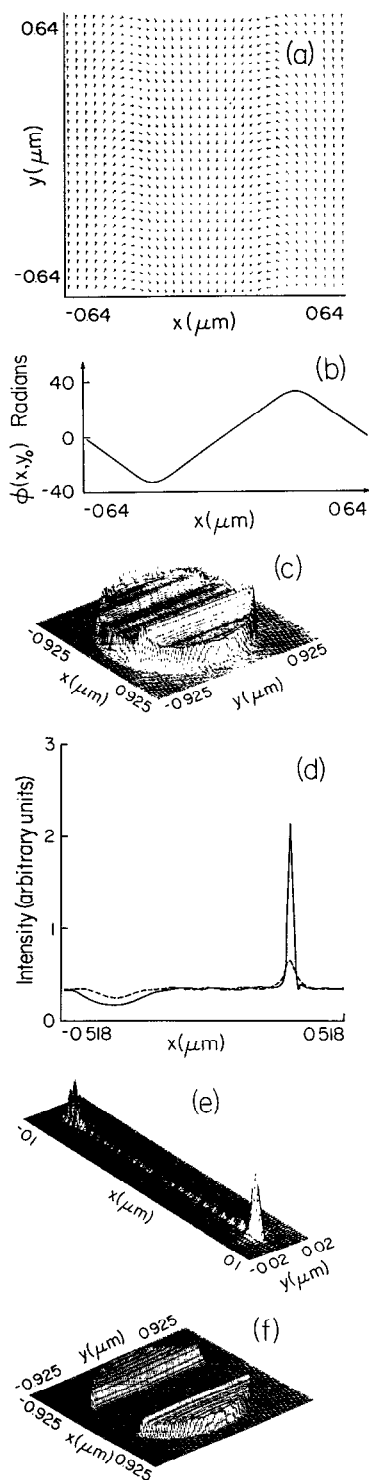


FIG. 2. (a) Pair of side-by-side Neel walls in a thin film with in-plane magnetization. The actual lattice used in the computations is  $256 \times 256$  with a lattice constant of  $50 \text{ \AA}$ . The assumed film thickness is  $\tau = 600 \text{ \AA}$  and the saturation magnetization of the sample is  $M_s = 1000 \text{ emu/cm}^3$ . (b) Plot of the phase function  $\Phi(x,y)$  vs  $x$  for a fixed (arbitrary) value of  $y$ . (c) Intensity distribution of the electron beam in the Fresnel mode at a defocus distance of  $0.37 \text{ mm}$ . The circle marks the boundary of the beam. The "bright" and "dark" lines are the images of the two side-by-side walls. (d) Cross sections of the intensity distribution patterns in the Fresnel mode, corresponding to defocus distances of  $0.925 \text{ mm}$  (solid curve) and  $0.37 \text{ mm}$  (dashed curve). (e) Intensity in the focal plane of a lens with  $f = 1.11 \text{ mm}$ . The lens is immediately behind the magnetic film and the beam diameter in the plane of the specimen is  $1.48 \text{ \mu m}$ . (f) Foucault image of the pair of Neel walls in (a), obtained by blocking the right half of the focal plane distribution in (e) and allowing the remaining electrons to propagate a distance of  $1.11 \text{ mm}$ .

Accordingly, the deflection angle for a uniform, normally incident beam on this sample is  $67.5$  microradians.

In the following examples several cases of practical interest are explored. Unless otherwise specified,  $L_x = L_y = 1.28 \text{ \mu m}$ ,  $\tau = 600 \text{ \AA}$ ,  $M_s = 1000 \text{ emu/cm}^3$ , and  $\lambda = 0.037 \text{ \AA}$ . The magnetization distribution is defined on a  $256 \times 256$  square lattice with a lattice constant of  $50 \text{ \AA}$ . The chosen distributions satisfy the periodic boundary conditions with smooth transitions at the boundaries. The structure of individual domain walls is described by the equation

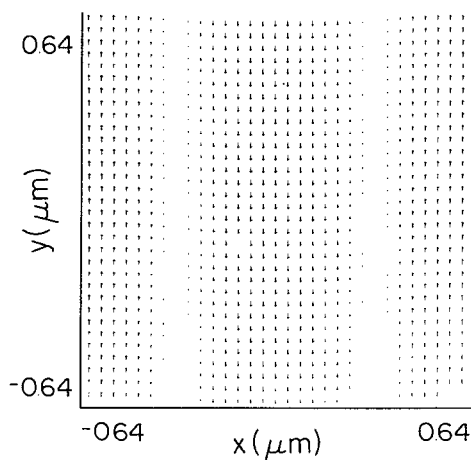


FIG. 3. Pair of side-by-side Bloch walls in a thin film with in-plane magnetization.

$$\Theta(x) = 2 \arctan \left[ \exp \left( \frac{x - x_0}{\Delta_w} \right) \right], \quad (17)$$

where  $x_0$  is the position of the center of the wall,  $\Delta_w$  is the wall thickness parameter, and  $\Theta$  is the angle of deviation of the magnetization vector relative to its orientation at  $x = -\infty$ . Unless specified to the contrary, the separation between adjacent walls is  $0.64 \text{ \mu m}$  and  $\Delta_w = 500 \text{ \AA}$ . The diffraction calculations reported in this paper are based on the standard methods of scalar diffraction theory<sup>9,10</sup> and require two Fourier transformations for the Fresnel mode of microscopy.

### A. Side-by-side walls in a thin film with in-plane magnetization

Consider the two  $180^\circ$  Neel walls shown in Fig. 2(a). (At least two walls are needed in parallel in order to achieve periodicity at the boundary.) The magnetization vector everywhere is in the plane of the film. For normally incident electrons, the phase function  $\Phi(x,y)$  is independent of  $y$ . A plot of  $\Phi(x,y)$  versus  $x$  for a fixed value of  $y$  is shown in Fig. 2(b). Figure 2(c) shows the calculated intensity pattern in the Fresnel mode at a defocus distance of  $0.37 \text{ mm}$ . The circular cross section of the electron beam with a diameter of  $1.48 \text{ \mu m}$  is also visible in this picture. As expected the wall on the right hand side gives rise to an intensity peak whereas the wall on the left hand side creates an intensity valley. Figure 2(d) shows cross sections of the intensity profiles at two different defocus distances. The solid curve corresponds to  $0.925 \text{ mm}$  of defocus whereas the dashed curve represents the intensity pattern at a defocus distance of  $0.37 \text{ mm}$ . The general features of these patterns are similar, but obvious differences in their detailed structure and relative contrasts may be noticed.

To investigate the image properties in the Foucault mode of Lorentz microscopy, we calculated the intensity pattern when a lens with focal length of  $f = 1.11 \text{ mm}$  is placed immediately behind the sample. Figure 2(e) shows the intensity distribution in the focal plane of the lens. The

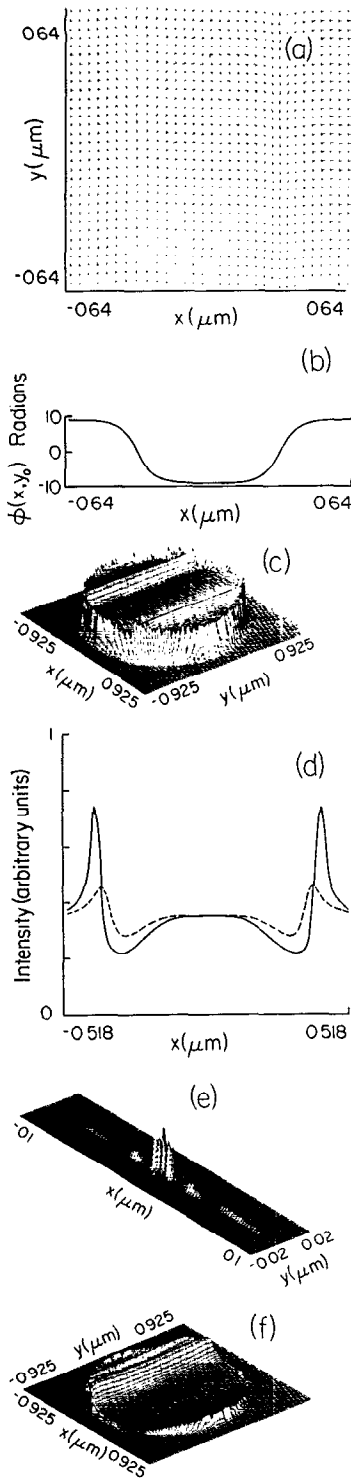


FIG. 4. (a) Pair of head-to-head/tail-to-tail walls in a thin film with in-plane magnetization. The actual lattice used in the computations is  $256 \times 256$  with a lattice constant of  $50 \text{ \AA}$ . The assumed film thickness is  $\tau = 600 \text{ \AA}$  and the saturation magnetization of the sample is  $M_s = 1000 \text{ emu/cm}^3$ . (b) Plot of the phase function  $\Phi(x,y)$  vs  $x$  for a fixed (arbitrary) value of  $y$ . (c) Intensity distribution of the electron beam in the Fresnel mode at a defocus distance of  $0.37 \text{ mm}$ . The circle marks the boundary of the beam. (d) Cross sections of the intensity distribution patterns in the Fresnel mode, corresponding to defocus distances of  $0.925 \text{ mm}$  (solid curve) and  $0.37 \text{ mm}$  (dashed curve). (e) Intensity pattern in the focal plane of a lens with  $f = 1.11 \text{ mm}$ . The lens is immediately behind the magnetic film and the beam diameter in the plane of the specimen is  $1.48 \text{ }\mu\text{m}$ . (f) Foucault image of the pair of walls in (a), obtained by blocking the left half of the focal plane distribution in (e) and allowing the remaining electrons to propagate a distance of  $1.11 \text{ mm}$ .

two peaks of this distribution correspond to the two regions of uniform magnetization along  $y$ . A relatively weak line between the two peaks is also visible in Fig. 2(e). If one blocks the right half of the focal plane and allows the remaining electrons to propagate a distance of  $1.11 \text{ mm}$ , one obtains the intensity pattern of Fig. 2(f). This is the Foucault image normally obtained in practice, showing clearly the effect of removing the central portion of the beam by means of spatial filtering in the frequency space.

Let us mention in passing that the results obtained here for a Neel wall apply equally to Bloch walls. Figure 3

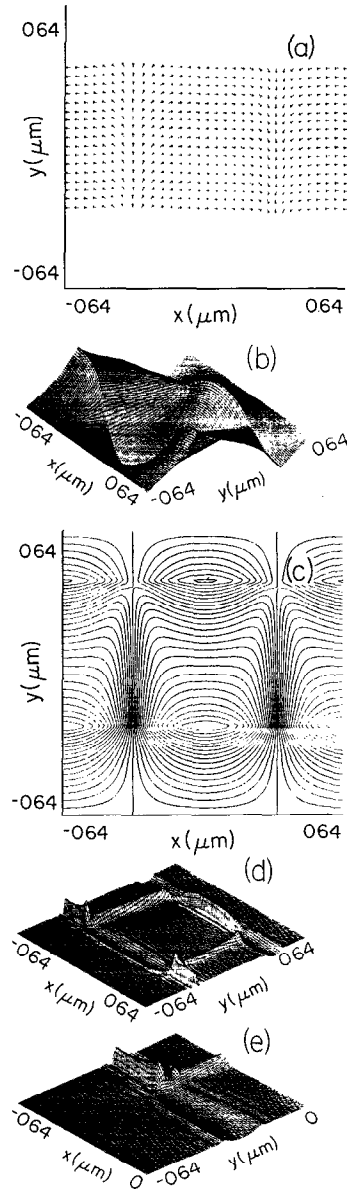


FIG. 5. (a) Pair of head-to-head/tail-to-tail walls on a narrow track. (b) Plot of the phase function  $\Phi(x,y)$ . The minimum/maximum values of the function are  $\pm 16.65$  radians. (c) Contour plot of  $\Phi(x,y)$ . (d) Intensity distribution corresponding to the Fresnel image at a defocus distance of  $0.925 \text{ mm}$ . (e) Magnified view of the lower left corner of (d).

shows the magnetization pattern for a pair of Bloch walls. In the case of Neel walls, what contributes to the image (and this is true for all modes of Lorentz microscopy that utilize electrons at normal incidence) is the component of magnetization along the  $y$  axis. As for the component along  $x$ , the Fourier transform of this component is everywhere parallel to the frequency vector  $\sigma$ , thus making no contributions to  $\Phi(x,y)$ . In the case of Bloch walls, the  $z$  component of magnetization is eliminated in the process of  $\mathbf{p} \times [\mathbf{p} \times \mathbf{m}(x,y)]$  calculation. Once again, the  $y$  component is solely responsible for the phase delay imparted to the electrons, rendering a Bloch wall indistinguishable from a Neel wall. The above argument breaks down when the impinging electrons are no longer perpendicular to the surface of the specimen, raising the possibility to differentiate between the two types of wall at oblique incidence.

## B. Head-to-head and tail-to-tail walls

Another simple magnetic structure is the  $180^\circ$  head-to-head (or tail-to-tail) wall, a pair of which are shown in

Fig. 4(a). The computed phase function  $\Phi(x,y)$  for this wall pair at normal incidence is shown in Fig. 4(b). Figure 4(c) is the corresponding intensity pattern in the Fresnel mode with 0.37 mm of defocus. Unlike the case of side-by-side walls, this Fresnel image contains identical patterns for the two walls. Each head-to-head or tail-to-tail wall whose magnetization remains in the plane of the sample gives rise to a bright line immediately following (or followed by) a dark line. Of course, one would arrive at the same qualitative conclusions following geometrical considerations based on the Lorentz law of force and the bending of electron trajectories. Quantitative descriptions of the line shapes and the exact contrast values, however, can only be obtained with a rigorous method based on the theory of diffraction, such as the one described in this paper. The solid and dashed curves in Fig. 4(d) show cross sections of the intensity pattern at defocus distances of 0.925 and 0.37 mm, respectively. Increasing the defocus distance in the Fresnel mode clearly increases the contrast. Figure 4(e) is the intensity pattern in the focal plane of the lens with  $f = 1.11$  mm. Blocking the left half of this pattern and allowing the remaining electrons to propagate a distance of 1.11 mm results in the intensity distribution of Fig. 4(f). This corresponds to the pattern obtained in the Foucault mode of imaging.

### C. Head-to-head walls on narrow track

An interesting experiment has been performed recently involving magnetic domains recorded on an etched track of finite width in a magnetic disk system.<sup>4</sup> The Fresnel image obtained in the experiment shows not only the recorded transitions along the track, but also the distribution of the stray magnetic field on the edges of the track. The situation is depicted in Fig. 5(a) which shows a pair of head-to-head/tail-to-tail walls on a  $0.64\text{-}\mu\text{m}$ -wide track along the  $x$  axis. The computed (normal-incidence) phase function  $\Phi(x,y)$  for this magnetization pattern is shown in Fig. 5(b) and a contour plot of  $\Phi(x,y)$  appears in Fig. 5(c). With an electron beam of diameter  $2.22\ \mu\text{m}$  and a defocus of 0.925 mm the Fresnel image shown in Fig. 5(d) is obtained. Note how the stray field near the edges of the track would create alternating patterns of bright and dark in a photographed image. A magnified view of the lower left corner of this pattern is shown in Fig. 5(e).

### D. Zigzag head-to-head wall

Figure 6(a) shows a zigzag head-to-head wall in a thin film medium with in-plane magnetization. The direction of magnetization at the wall center is assumed to be perpendicular to the plane of the film. As indicated in the figure, the period and the amplitude of the zigzag are defined as its peak-to-peak separation along the wall and across the wall, respectively. For the computation results that follow, the zigzag amplitude was fixed at  $0.2\ \mu\text{m}$ . The case of a zigzag with the relatively large period of  $0.426\ \mu\text{m}$  is shown in Figs. 6(b) and 6(c) which respectively depict the corresponding (normal-incidence) phase function  $\Phi(x,y)$  and the intensity distribution in the Fresnel mode with a defo-

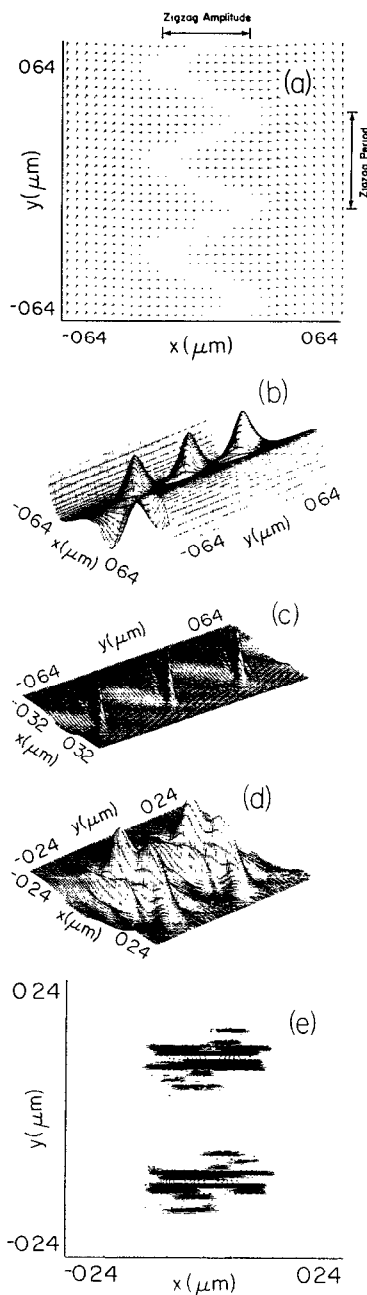


FIG. 6. (a) Zigzag head-to-head wall in a thin film with in-plane magnetization. The magnetization within the wall region is perpendicular to the plane of the film. (b) Computed  $\Phi(x,y)$  for a zigzag wall with amplitude of  $0.2\ \mu\text{m}$  and period of  $0.426\ \mu\text{m}$ . Minimum and maximum values of the function are  $-6.47$  rad and  $+6.54$  rad, respectively. (c) Intensity distribution corresponding to the Fresnel image with 0.925 mm of defocus. (d) Fresnel intensity pattern for a zigzag wall with an amplitude of  $0.2\ \mu\text{m}$  and a period of  $0.213\ \mu\text{m}$ . The defocus distance is 1.295 mm. Only two periods of the zigzag are within the depicted region. (e) Contour plot of the pattern in (d).

cus of 0.925 mm. The region of space shown in these figures contains three full periods of the zigzag wall. If the zigzag period is now reduced to  $0.213\ \mu\text{m}$ , the pattern becomes more complex, as can be seen in the Fresnel pattern of Fig. 6(d) which has a defocus of 1.295 mm. [See also the corresponding contour plot in Fig. 6(e).] Note that the region depicted in Figs. 6(d) and 6(e) contains only two periods of the zigzag.

Another possible structure for the zigzag wall is shown in Fig. 7(a) where, in contrast to the preceding case, the wall magnetization lies in the plane of the film. For numerical calculations, the zigzag amplitude and period were chosen to be  $0.2\ \mu\text{m}$  and  $0.213\ \mu\text{m}$ , respectively. Figure 7(b) shows  $\Phi(x,y)$  at normal incidence for a region of space containing six periods of the zigzag. The corresponding Fresnel pattern with 1.295 mm of defocus is shown in Fig. 7(c) [see also the contour plot in Fig. 7(d)]. The

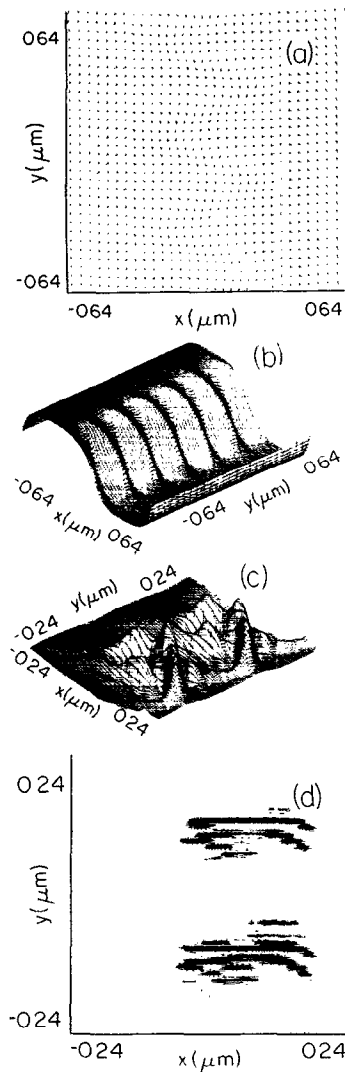


FIG. 7. (a) Zigzag head-to-head wall in a thin film with in-plane magnetization. The magnetization within the wall region is also in the plane of the film. (b) Computed  $\Phi(x,y)$  for the zigzag amplitude and period of 0.2 and 0.213  $\mu\text{m}$ , respectively. The minimum/maximum values of the function are  $\pm 9$  rad. (c) Intensity distribution in the Fresnel image with 1.295 mm of defocus. Only two periods of the zigzag are within the depicted region. (d) Contour plot of the pattern in (c).

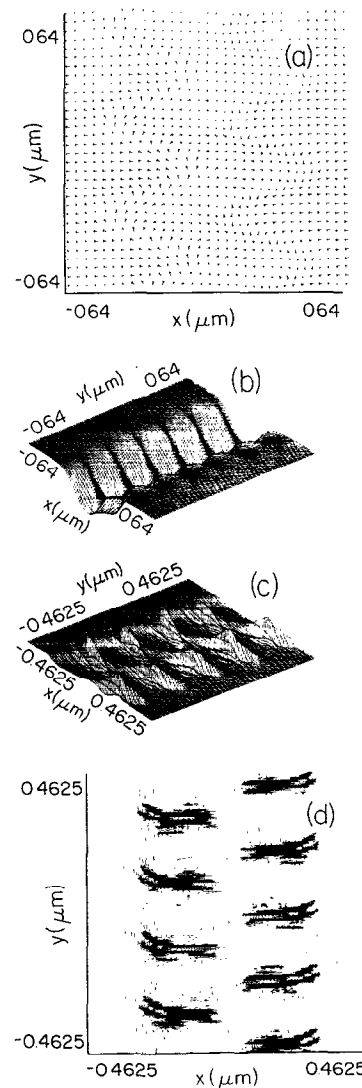


FIG. 8. (a) Pair of zigzag walls in a thin film with in-plane magnetization. The magnetization within the wall regions is also in the plane of the film. (b) Computed  $\Phi(x,y)$  for the zigzag amplitude of 0.2  $\mu\text{m}$ , zigzag period of 0.213  $\mu\text{m}$ , and center-to-center wall separation of 0.256  $\mu\text{m}$ . Minimum and maximum values of the function are  $-11.9$  and  $+3.7$  rad, respectively. (c) Intensity distribution in the Fresnel image with 0.925 mm of defocus. (d) Contour plot of the pattern in (c).

regions depicted in these figures contain only two periods of the zigzag.

Finally, consider the pair of zigzag walls in Fig. 8(a). Together, these walls create a winding stripe of reverse magnetization in the central region of the specimen. For numerical calculations, the walls were assumed to have zigzag amplitude of 0.2  $\mu\text{m}$ , zigzag period of 0.213  $\mu\text{m}$ , and center-to-center separation of 0.256  $\mu\text{m}$ . The phase function  $\Phi(x,y)$  at normal incidence is shown in Fig. 8(b), and the intensity pattern in the Fresnel mode with 0.925 mm of defocus is shown in Fig. 8(c) [see also the contour plot of this intensity distribution in Fig. 8(d)].

### E. Circular domain in a thin film with perpendicular magnetization

Figure 9(a) shows the magnetization distribution for a circular domain in a perpendicular medium. Inside the domain the magnetization vector  $\mathbf{m}$  is along  $-z$  whereas in the outside region  $\mathbf{m}$  is along  $+z$ . In the state of minimum magnetostatic wall energy shown in Fig. 9(a), the wall magnetization everywhere is parallel to the wall itself. The computed  $\Phi(x,y)$  for a domain of this type with a diameter of 0.64  $\mu\text{m}$  and wall thickness parameter of  $\Delta_w = 100$   $\text{\AA}$  is shown in Fig. 9(b), and the corresponding Fresnel pattern

with a defocus of 0.37 mm is shown in Fig. 9(c). The Fresnel pattern in this case is a bright ring whose radius, depending on the sense of magnetization within the wall, is either slightly less or slightly more than the radius of the magnetic domain itself. When the electron beam is incident at an oblique angle with  $p_x = 0.5$ ,  $p_y = 0$  and  $p_z = 0.866$ , Figs. 9(d) and 9(e) are obtained. These figures show, respectively, the phase function  $\Phi(x,y)$  and the Fresnel pattern with 0.37 mm of defocus. Note that the Fresnel pattern in this case is no longer symmetric with respect to the center of the domain. The brightness of the ring has increased on one side and decreased on the other, in agreement with the experimental results reported for the magneto-optical recording media.<sup>3</sup>

A more complex wall structure for circular domains is depicted in Fig. 10(a). Here the wall is not in a state of minimum magnetostatic energy and shows several twists known as vertical Bloch lines. The corresponding (normal-incidence) phase function and the Fresnel pattern with 0.37 mm of defocus are shown in Figs. 10(b) and 10(c), respectively. Figure 10(d) shows the Fresnel pattern at oblique incidence with  $\mathbf{p} = (0.5, 0, 0.866)$ . Compared with Fig. 9(e), the bright and dark halves of the ring are somewhat more pronounced in the present case.

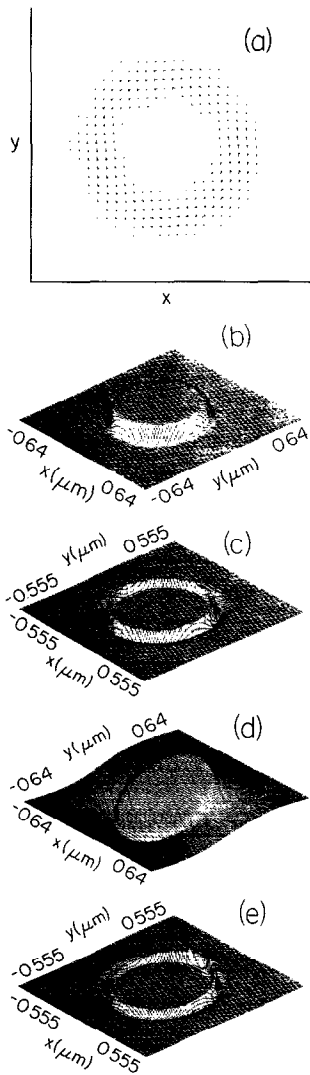


FIG. 9. (a) Circular domain in a thin film with perpendicular magnetization. The wall magnetization everywhere is parallel to the wall itself. (b) Computed  $\Phi(x,y)$  at normal incidence for a domain diameter of  $0.64 \mu\text{m}$  and a wall thickness parameter  $\Delta_w = 100 \text{ \AA}$ . The minimum and maximum values of the function are  $-0.7$  rad and  $+2.9$  rad, respectively. (c) Intensity distribution for the Fresnel pattern at  $0.37$  mm of defocus. (d) Computed  $\Phi(x,y)$  at oblique incidence with  $\mathbf{p} = (0.5, 0, 0.866)$ . (e) Fresnel image at oblique incidence. The defocus distance is  $0.37$  mm.

### F. Vortices in a thin film medium with in-plane magnetization

Figure 11(a) is a plot of four vortices at the centers of the four quadrants of the lattice representing a thin magnetic film. (Four is the smallest possible number of vortices within the unit cell, given the constraint of periodic boundary conditions). The computed phase function  $\Phi(x,y)$  for this magnetization pattern is shown in Fig. 11(b) and the Fresnel patterns at defocus distances of  $0.925$  mm and  $0.37$  mm are shown in Figs. 11(c) and 11(d), respectively. The intensity patterns reveal that a counterclockwise vortex acts as a positive lens by bringing the electron beam to a focus, whereas a clockwise vortex, by diffracting the rays away from each other and creating a dark spot in the image, acts as a negative lens. Figure 11(e) gives a magnified view of the central region of the diffraction pattern of Fig. 11(d). The corresponding magnetization distribution in this region exhibits a sort of saddle point behavior and the locations of intensity peaks and valleys near the center of Fig. 11(e) are consistent with the expected geometrical behavior of the electrons in this region.

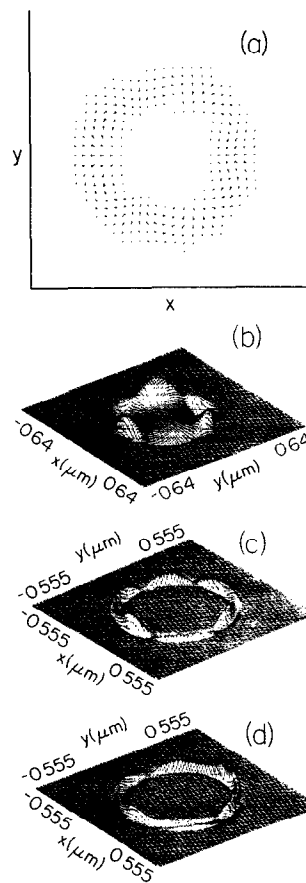


FIG. 10. (a) Circular domain in a perpendicular film. The wall magnetization contains several twists or vertical Bloch lines. (b) Computed  $\Phi(x,y)$  at normal incidence for a domain diameter of  $0.64 \mu\text{m}$  and a wall thickness parameter  $\Delta_w = 100 \text{ \AA}$ . Minimum/maximum values of the function are  $\pm 2.67$  radians. (c) Fresnel pattern at normal incidence with  $0.37$  mm of defocus. (d) Fresnel image at oblique incidence with  $\mathbf{p} = (0.5, 0, 0.866)$  and  $0.37$  mm of defocus.

### G. Sinks and sources in thin film medium with in-plane magnetization

Consider the magnetization pattern of Fig. 12(a) which consists of two "sinks" and two "sources" at the centers of the four quadrants of the lattice. Figure 12(b) shows the computed (normal-incidence) phase function  $\Phi(x,y)$  for this magnetization distribution. In the vicinity of the sources and the sinks, the phase function is flat and featureless, although it shows complex structure near the saddle points. Thus a technique such as Differential Phase Contrast, which uses the electron microscope in the scanning transmission mode and attempts to reconstruct the state of magnetization of the sample point by point, will miss the sinks and sources altogether. That is not to say that other techniques fare better in this respect, but, by providing a global view, they might at least give clues as to the nature and the whereabouts of the sinks and sources. Figure 12(c) is the Fresnel image of the magnetization distribution of Fig. 12(a) at a defocus distance of  $0.37$  mm. Notice that only the boundaries between adjacent sinks and/or sources stand out in this picture. Figure 12(d) gives a magnified view of the central region of this figure, where the structure of the boundary may be observed in some detail. Finally, Fig. 12(e) shows the Fresnel pattern obtained at oblique incidence with  $\mathbf{p} = (0.5, 0, 0.866)$ . The sinks and sources which were absent in the previous figure now make an appearance.

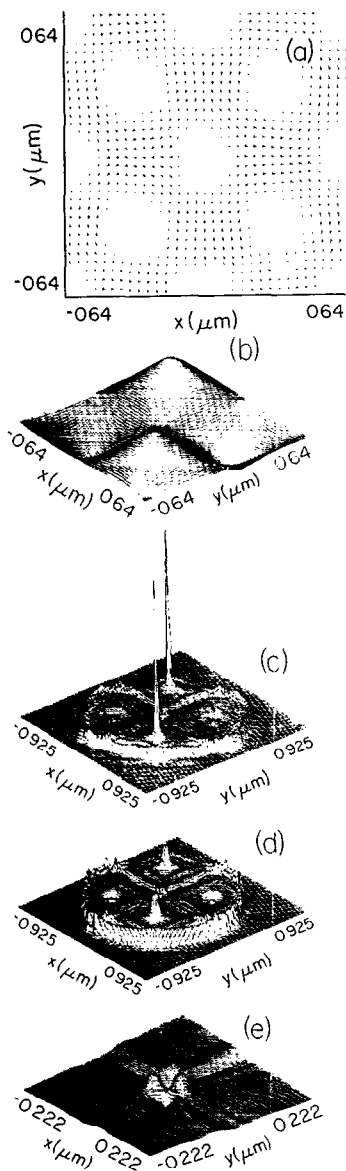


FIG. 11. (a) Four vortices in a thin film with in-plane magnetization. The regions with an out-of-plane component of magnetization (i.e., cores as well as singularities in between the vortices) have a Gaussian shape with  $1/e$  radius of  $500 \text{ \AA}$ . (b) Plot of the phase function  $\Phi(x,y)$  when the beam is normally incident on the specimen. The minimum/maximum values of the function are  $\pm 35.82$  radians. (c) Intensity pattern of the electron beam in the Fresnel mode with  $0.925 \text{ mm}$  of defocus. (d) Intensity pattern in the Fresnel mode with  $0.37 \text{ mm}$  of defocus. (e) Magnified view of the central region of (d).

#### H. Magnetization ripple in medium with in-plane magnetization

The magnetization pattern in Fig. 13(a) is obtained by adding a certain amount of random noise (ripple) to a uniform distribution of magnetization vectors. The simulated ripple is created by randomly and independently adding a value in the interval  $(-20^\circ, +20^\circ)$  to the orientation angles of individual dipole moments. The phase function in Fig. 13(b) and the Fresnel image in Fig. 13(c) correspond to the region whose magnetization is depicted in Fig. 13(a). Also shown is the contour plot of the Fresnel image in Fig. 13(d). Obviously, the relationship between the magnetization pattern and its Fresnel image is not a simple one. This is partly due to stray magnetic fields in and around the sample, and partly the result of interference amongst the neighboring rays of the electron beam. The complexity of the relationship between the magnetization ripple and its Fresnel image increases with increasing spatial frequency of the pattern, making interpretations of the image based on simple geometrical considerations exceedingly unreliable.

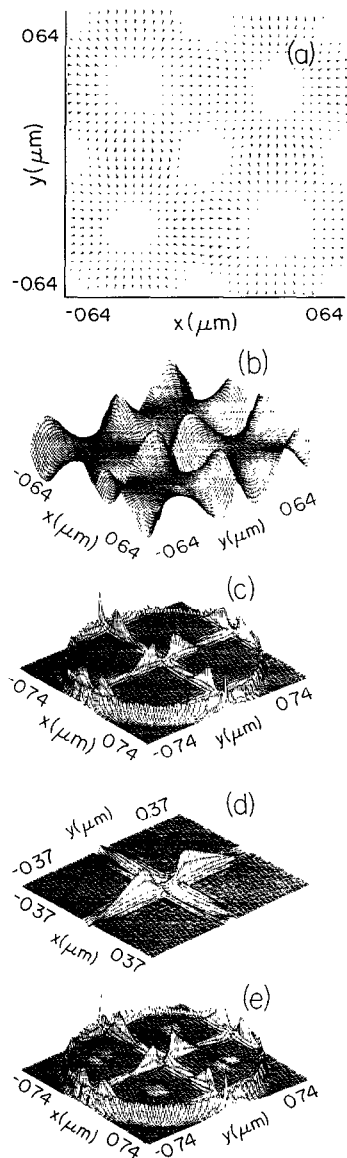


FIG. 12. (a) Two sources and two sinks in a thin film with in-plane magnetization. The regions with out-of-plane magnetization (i.e., cores as well as singularities in between sinks and sources) have a Gaussian shape with  $1/e$  radius of  $500 \text{ \AA}$ . (b) Plot of the phase function  $\Phi(x,y)$ . The minimum and the maximum values of  $\Phi$  are  $-4.4$  and  $+4.4$  rad, respectively. (c) The intensity pattern of the electron beam in the Fresnel mode with a defocus distance of  $0.37 \text{ mm}$ . (d) Magnified view of the central region of the pattern in (c). (e) Fresnel image at oblique incidence. The beam is turned away from the normal by  $30^\circ$  ( $p_x = 0.5$ ,  $p_y = 0$ ,  $p_z = 0.866$ ) and the defocus is  $0.37 \text{ mm}$ .

#### IV. CONCLUDING REMARKS

A powerful and accurate technique for computing the phase modulation of the electron beam in Lorentz electron microscopy has been described. The results are quite general and can be used to compute the electron diffraction patterns under any of the several possible modes of Lorentz microscopy. Numerical examples were given that considered normally incident electron beams as well as beams incident at an oblique angle. These examples analyzed both the Fresnel and Foucault modes of imaging as well as small angle electron diffraction patterns. On a VAX workstation, the calculation of each phase function on a  $256 \times 256$  lattice was completed in about 50 seconds. Computation of the Fresnel diffraction patterns on a  $512 \times 512$  lattice required two fast Fourier transforms and took a total time of approximately 2.5 minutes.

#### ACKNOWLEDGMENTS

Thanks are due to Professor J. N. Chapman of the University of Glasgow, to Dr. P. S. Alexopoulos and Dr. I.

R. McFadyen, both of the IBM's Almaden Research Center, and to Professor Roscoe Giles of Boston University for many helpful discussions. This work has been supported by a grant from the IBM Corporation and by the Optical Data Storage Center at the University of Arizona.

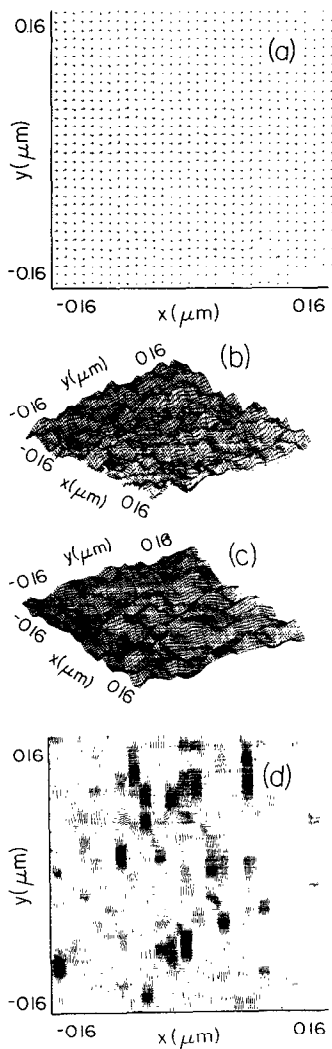


FIG. 13. (a) The magnetization pattern in the central region of the film. The orientation angles of the dipoles deviate from the  $x$  axis by a random number in the interval  $[-20^\circ, +20^\circ]$ . (b) Plot of  $\Phi(x,y)$  at normal incidence. The minimum and the maximum values of  $\Phi$  are  $-0.53$  and  $+0.55$  rad, respectively. (c) Fresnel image of the magnetization pattern shown in (a). The defocus distance is  $0.925$  mm. (d) Contour plot of the Fresnel pattern in (c).

- <sup>1</sup>J. N. Chapman, *J. Phys. D* **17**, 623 (1984).
- <sup>2</sup>J. N. Chapman and G. R. Morrison, *J. Mag. Mag. Mater.* **35**, 254 (1983).
- <sup>3</sup>J. C. Suits, R. H. Geiss, C. J. Lin, D. Rugar, and A. E. Bell, *J. Appl. Phys.* **61**, 3509 (1987).
- <sup>4</sup>T. Nguyen, P. Alexopoulos, C. Hwang, S. Lambert, and I. Sanders, *IEEE Trans. Magn.* **24**, 2733 (1988).
- <sup>5</sup>S. Tsukahara, *JARECT*, **15**, Recent Magnetism for Electronics, edited by Y. Sakurai (1984).
- <sup>6</sup>I. R. McFadyen, Proceedings of the 47th Annual Meeting of the Electron Microscopy Society of America, edited by G. W. Bailey (San Francisco Press Inc., San Francisco, 1989).
- <sup>7</sup>Y. Aharonov and D. Bohm, *Phys. Rev.* **115**, 485 (1959).
- <sup>8</sup>M. Mansuripur and R. Giles, *IEEE Trans. Magn.* **24**, 2326 (1988).
- <sup>9</sup>M. V. Klein, *Optics* (Wiley, New York, 1970).
- <sup>10</sup>M. Mansuripur, *J. Opt. Soc. Am. A* **6**, 786 (1989).